PAPER

Check for updates

A novel quartz-crystal microbalance humidity sensor based on solution-processible indium oxide quantum dots†

Hao Kan,[ab] Min Li,[c] Hui Li,[a] Chong Li,[a] Jian Zhou,[d] Chen Fu,[a] Jingting Luo [ID] *[a] and Yongqing Fu [ID] [e]

Having a large surface area, like the quantum confinement effect also caused by the nano-level size of quantum dots (QDs), creates fantastic potential for humidity sensing. A high concentration of surface adsorption sites initiates an increased response. Porosity between QDs allows fast water vapor penetration and outflow. Here, a quartz-crystal microbalance (QCM) humidity sensor was prepared using indium oxide (In_2O_3) QDs, synthesized *via* a solvothermal method. After the In_2O_3 QDs were directly spin-coated onto the QCM, an annealing process removed organic long chains and exposed more moisture adsorption sites on the surfaces of the QDs. The annealed QCM humidity sensor exhibited high sensitivity (56.3 Hz per %RH at 86.3% RH), with a fast response/recovery time (14 s/16 s). Long carbon chains were broken down, and hydrogen-bonded hydroxyl groups were chemisorbed to the QDs. The chemical reaction was reduced by these chemisorbed hydrogen-bonded hydroxyl groups. Mass change was mostly caused by fast multilayer physisorption. Thus, the transducer can effectively and precisely monitor the moisture from a person's breath. In_2O_3 QD-modified QCM sensors demonstrate promising humidity-sensing applications in daily life.

Introduction

Humidity sensors have been widely used in the fields of chemistry, electronics, food storage, mining, meteorology, agriculture, medicine, and others.[1–4] Accurate and real-time monitoring of humidity is also critical for human safety and social activities. Therefore, it is critically required to develop a high-performance, repeatable and low-cost humidity sensor. So far, various sensing technologies have been developed for humidity sensors, including resistance, optical, magnetic, acoustic capacitance and thermal sensing, among others.[5–9] Among these, the quartz crystal microbalance (QCM) is one of the most promising and key technologies due to its merits such

[a]*Shenzhen Key Laboratory of Advanced Thin Films and Applications, College of Physics and Optoelectronic Engineering, Shenzhen University, 518060, Shenzhen, China. E-mail: luojt@szu.edu.cn*

[b]*Key Laboratory of Optoelectronic Devices and Systems of Ministry of Education and Guangdong Province, College of Optoelectronic Engineering, Shenzhen University, 518060, Shenzhen, China*

[c]*School of Electrical Engineering, Nanjing Institute of Industry Technology, 210023, Nanjing, China*

[d]*State Key Laboratory of Advanced Design and Manufacturing for Vehicle Body, College of Mechanical and Vehicle Engineering, Hunan University, Changsha 410082, China*

[e]*Faculty of Engineering and Environment, Northumbria University, Newcastle Upon Tyne, Newcastle NE1 8ST, UK*

† Electronic supplementary information (ESI) available. See DOI: 10.1039/c9ra06385d

as low power consumption, easy operation, low cost, good sensitivity and extremely trace mass detection. By monitoring the shifts of the resonance frequency in real time, the mass change caused by water molecules can be precisely detected using the Sauerbrey equation.[10] Therefore, QCM sensors have been extensively researched as humidity sensors by more and more researchers.[11–18]

Based on the above advantages, various sensitive materials, such as 0-dimensional (0D) QDs, 1-dimensional (1D) nanowires, graphene, reduced graphene oxide (RGO), black phosphorus and many types of polymers have been applied on the surface of QCM humidity sensors.[19–26] Obviously, these nanomaterials provide numerous reactive sites due to their larger specific surface areas, resulting in improved humidity sensing performance. Among them, 0D QDs exhibit wide-ranging potential applications in the field of humidity sensors due to their low cost, large specific surface areas and easy solution processing.[27–29] For example, Sun *et al.* prepared well-crystallized black phosphorus QDs from bulk black phosphorus using a kitchen blender, and the sensor using the black phosphorus QDs showed outstanding humidity sensing performance.[30] A flexible humidity sensor fabricated using graphene QDs was reported by Hosseini *et al.*, and the response of the transducer was quite high, with good selectivity and flexibility.[31] Another QCM humidity sensor based on ZnO QD sensitive film was reported by Sakly *et al.*, and it exhibited high sensitivity, fast response/recovery speed and outstanding long-term stability.[32]

Therefore, QDs with high specific surface area are a very promising type of humidity-sensitive material.

Based on the discussion above, in the present work, we fabricated a QCM humidity sensor based on In$_2$O$_3$ QDs. The In$_2$O$_3$ QDs were spin-coated on the top of the electrodes of QCMs in the form of thin films, then the devices were annealed at 300 °C in air for one hour to remove long-chain carbons on the surface of the QDs. The humidity sensing performance of the QCM sensor was characterized at room temperature, from 11.3% to 84.3% relative humidity (RH). The sensor showed remarkable sensing characteristics, including high sensitivity (56.4 Hz per %RH), fast response/recovery time (14 s/16 s), good stability and excellent selectivity for moisture. We believe this work provides a simple and easy way to fabricate a novel QCM humidity sensor based on In$_2$O$_3$ QDs.

Experimental section

In$_2$O$_3$ QD synthesis and device preparation

The In$_2$O$_3$ QDs were synthesized via a modified method employing oleic acid (OA) and oleylamine (OLA) as the surfactants.[33] Briefly, 0.146 g indium acetate, 12.5 mL OLA and 5 mL OA were mixed inside a three-necked flask. The mixture was heated under vacuum at 90 °C until the indium acetate was completely dissolved. Then, the solution was kept under nitrogen atmosphere and heated to 240 °C for 30 min. Finally, In$_2$O$_3$ QDs were washed with ethanol and toluene, and eventually dispersed in toluene with a concentration of 20 mg mL^{-1}.

The QCM devices with a resonant frequency of 8 MHz were purchased from Wuhan Hi-Trusty Electronics Co., Ltd., China. They consisted of an AT-cut quartz crystal (8 mm in diameter) and silver electrodes (5 mm in diameter) on both sides (Fig. 1a). Before preparing In$_2$O$_3$ QD film, all the QCM devices were washed with ethanol and deionized water, then dried with nitrogen. The film-coated QCM sensors were produced by spin-coating method and post-annealing process (Fig. 1b). Specifically, 20 μL In$_2$O$_3$ QD solution was spin-coated onto the QCM device at 1200 rpm for 45 s. To remove the organic long chains from the surface of the In$_2$O$_3$ QDs, an annealing process was carried out in air at 300 °C for 1 h. This procedure for fabricating the QCM humidity sensor is shown in Fig. 1b. To study the influence of the amount of deposited In$_2$O$_3$ QDs on sensing performance, three sensors with different deposition repeat cycles (2, 4, 6 times) were prepared, designated as QCM-1, QCM-2 and QCM-3, respectively. The resonant frequency and the frequency after coating with the film were measured, and the mass of the In$_2$O$_3$ QDs deposited on the electrode of QCMs was calculated using the Sauerbrey equation.[10] All the detailed parameters of the samples are listed in Table 1.
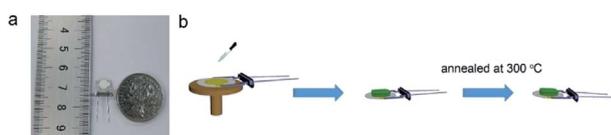

Fig. 1 (a) A photograph of the QCM device. (b) The fabrication procedure of the QCM humidity sensor based on In$_2$O$_3$ QDs.

Table 1 Preparation parameters of the fabricated samples

Sample	Fundamental frequency (Hz)	Frequency shift (Hz)	Load mass (ng)
QCM-1	7 999 890	−7266	9852
QCM-2	7 999 867	−14955	19 794
QCM-3	7 999 799	−21004	28 479

Sensing measurement

The schematic diagram of the experiment apparatus for the QCM humidity measurement is given in Fig. 2. It was composed of the QCM humidity sensor, humidity sources, a computer and QCM-I (Microvacuum Ltd., Hungary). Saturated solutions of LiCl, MgCl$_2$, K$_2$CO$_3$, NaBr, NaCl and KCl were prepared, which could provide different humidity environments in a conical flask, with RH levels of 11.3%, 32.8%, 43.2%, 57.6%, 75.3% and 84.3% RH, respectively. The response time was defined as the time for the frequency change to approach 90% of the total frequency change, and the recovery time was defined as the time it returned to 10% of the total frequency change. All the tests were performed at the ambient temperature of 25 °C.

Characterization

X-ray diffraction (XRD) analysis of the QD films was performed using a diffractometer (MAXima XXRD-7000, Shimadzu, Japan) with Cu Kα radiation. The optical absorption spectra of the QDs were measured using a PerkinElmer Lambda 950 UV/vis/NIR spectrometer. Surface morphologies of the QD samples were characterized using a scanning electron microscope (SEM, Zeiss Supra 55 microscope). High-resolution transmission electron microscopy (HR-TEM) was carried out using a JEOL-2100 microscope. The Fourier transform infrared (FTIR) spectroscopy was performed using a VERTEX 70 (Bruker, Germany).

Results and discussion

Fig. 3a shows the crystallization characteristics of the In$_2$O$_3$ QDs. The XRD pattern of the synthesized In$_2$O$_3$ QDs is in good agreement with the standard diffraction results listed in the JCPDS card (no. 65-3170), indicating the synthesized QDs have good crystallinity, and no other impurities appear. Fig. 3b shows a TEM image of In$_2$O$_3$ QDs. The In$_2$O$_3$ QDs were
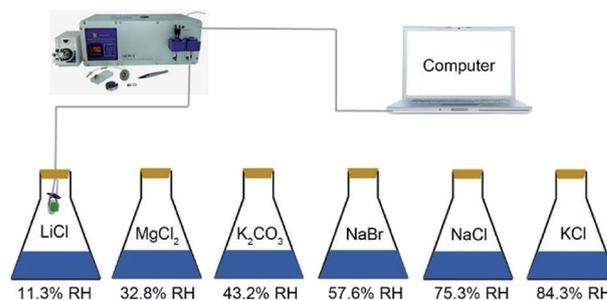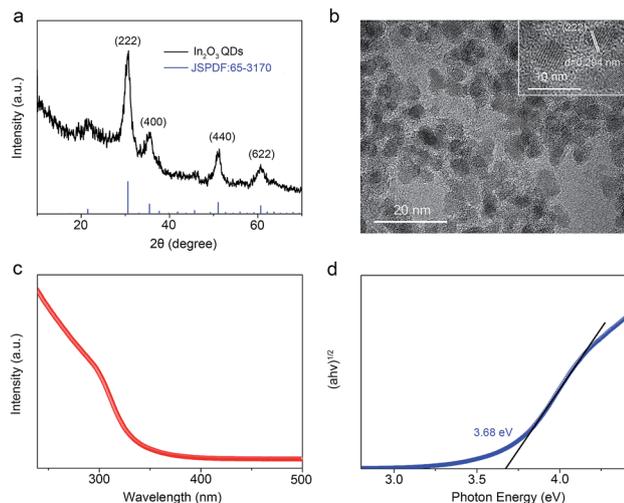

Fig. 2 A schematic diagram of the QCM humidity test system.

Fig. 3 (a) XRD patterns of the as-synthesized In_2O_3 QDs. (b) A TEM image of the In_2O_3 QDs; the inset is a HRTEM image of the In_2O_3 QDs. (c) The UV-vis absorption spectrum of the as-synthesized In_2O_3 QDs. (d) The bandgap of the as-synthesized In_2O_3 QDs.

Fig. 4 The nitrogen adsorption and desorption isotherms of In_2O_3 QDs.

uniformly dispersed and had an average diameter of 3.9 nm. This indicates that the diameter of the as-synthesized In_2O_3 QDs is less than twice the Bohr exciton radius of In_2O_3 (2.14 nm), confirming that the as-synthesized In_2O_3 has quantum size.[34,35] The transparent lattice fringes of atomic spacing associated with the (222) plane of the In_2O_3 phase can also be observed, as shown in the inset of Fig. 3b. This demonstrates that the In_2O_3 QDs have good crystallinity. Fig. 3c shows the absorption spectrum of as-synthesized In_2O_3 QDs in hexane. The band gap of as-synthesized In_2O_3 QDs calculated by the Tauc model is about 3.68 eV (shown in Fig. 3d), which is larger than that of bulk In_2O_3 (2.93 ± 0.15 eV). This result indicates that the as-synthesized In_2O_3 QDs have quantum confinement effect. As shown in Fig. 4, the nitrogen adsorption and desorption isotherm curves of In_2O_3 QDs were investigated. The surface area of In_2O_3 QDs is calculated to be about 63.9 $m^2 g^{-1}$ through the Brunauer–Emmett–Teller theory. As is known, high specific surface area can provide more active sites to promote the adsorption of water molecules, thus improving the humidity sensing.

The as-synthesized In_2O_3 QDs were capped with organic long-chain OA and OLA, and these hydrophobic organic long-chain molecules can inhibit water molecules from being adsorbed onto the surface of In_2O_3 QDs.[36,37] To remove the organic long chains, the In_2O_3 QD films should be annealed at 300 °C in air. In order to study the effect of the annealing process on the QDs, we use FTIR to analyse the In_2O_3 QD films before and after annealing, and the results are shown in Fig. 5. Compared to the as-prepared In_2O_3 QD film (red line), the characteristic absorption peaks of the aliphatic C–H stretching bands (2850–2920 cm^{-1}) disappeared after annealing (blue line), indicating that most of the surface-capped OA and OLA ligands around the In_2O_3 QDs have been removed.[18] As expected, after the annealing process, a very strong characteristic peak at around 3445 cm^{-1} appeared (blue line), which is
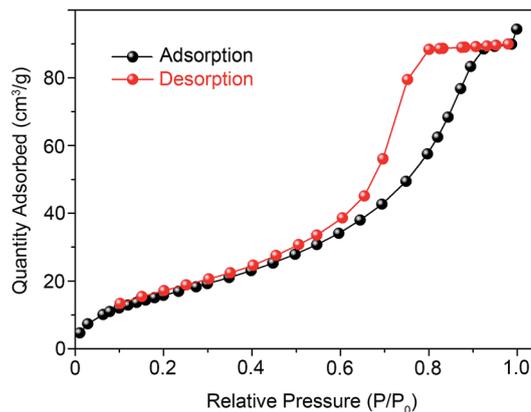
attributed to the hydrogen-bonded hydroxyl groups adsorbed on the In_2O_3 QDs. Results indicate that the In_2O_3 QD film has outstanding hydrophilicity after annealing.

The SEM morphologies of the In_2O_3 QD films before and after annealing were compared (QCM-3). Fig. 6a is the SEM image of the as-deposited In_2O_3 QD film showing holes, which may be caused by the evaporation of solvent during the film formation process. The In_2O_3 QD film is shown after annealing at 300 °C for 1 h in Fig. 6b. The corresponding element mapping obtained from energy dispersive X-ray spectroscopy is shown in Fig. 6a and b. The elements of In and O were uniformly dispersed, which indicates that the QDs were uniformly deposited on top of the QCM electrode. To better understand the influence of the surface morphology of In_2O_3 QDs films before and after annealing (QCM-3), the high-magnification SEM of films is shown in Fig. S1e and f,† respectively. Before annealing, the film is rough and shows no obvious cracks. After the film was annealed at 300 °C for 1 h, the QD film became smoother, but with some tiny cracks, which were generated owing to the densification with stress relaxation and the removal of organic long-chain ligands during the annealing
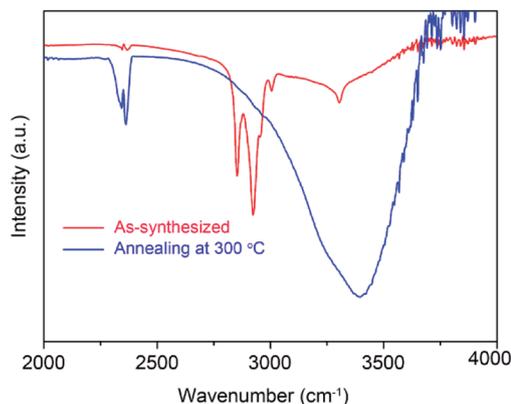

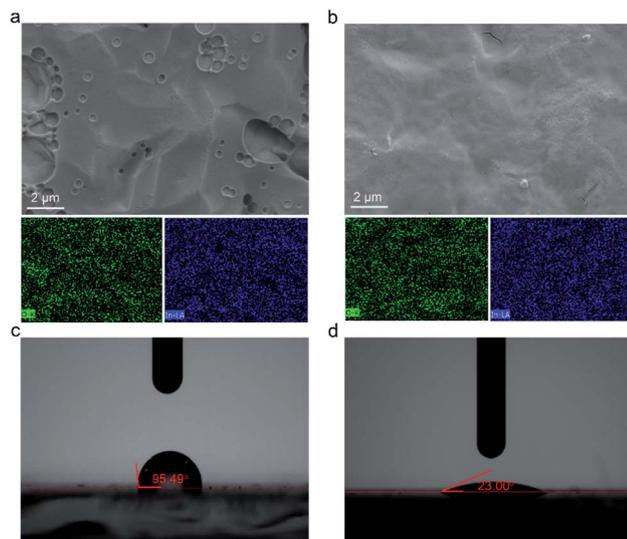**Fig. 5** FTIR spectra of untreated and annealed In_2O_3 QD films (QCM-3).

Fig. 6 (a) The as-prepared In$_2$O$_3$ QD film (QCM-3) before annealing. (b) The In$_2$O$_3$ QD film after annealing at 300 °C for 1 h (QCM-3). Contact angle measurements of (c) as-prepared In$_2$O$_3$ QD film (QCM-3 before annealing) and (d) In$_2$O$_3$ QD film after annealing (QCM-3).

process. This porous film is beneficial for the adsorption and diffusion of water molecules.

Fig. 6c and d show the wettability behaviours of In$_2$O$_3$ QD film before and after annealing (QCM-3). The contact angle of the as-deposited QD film is 95.49° (Fig. 6c). This is due to the hydrophobicity of the surface-capped organic long chains. After the annealing process, the contact angle of the In$_2$O$_3$ QD sensing film is as low as 23.00° (Fig. 6d). This value verifies the excellent hydrophilicity of the In$_2$O$_3$ QD sensing film. These results are consistent with FTIR spectra. Also, the results of FTIR and contact angle measurements suggest that the prepared QCM humidity sensor based on In$_2$O$_3$ QDs will have good humidity sensitivity.

The humidity sensitivity of the In$_2$O$_3$ QD-based QCM sensor was quantified by changing the RH level in different saturated solutions in conical flasks and measuring the changes of resonance frequency. Fig. 7a shows the relationship between frequency shifts $vs.$ RH for three sensors, with test RH between 11.3% and 84.3%. As seen in the figure, the resonant frequency of all the sensors decreased with the RH increase. The frequency shifts are 1550 Hz, 3100 Hz and 4750 Hz for the three QCM
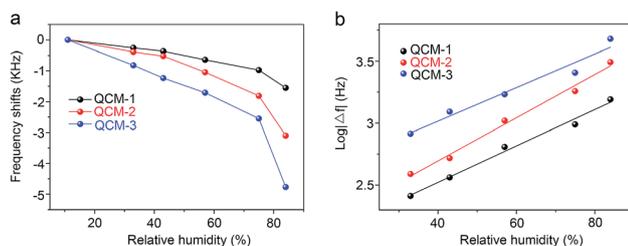

Fig. 7 (a) The relationships between the frequency shifts of all the sensors. (b) The linear fitting curves of log |Δf| $versus$ humidity for all the sensors.
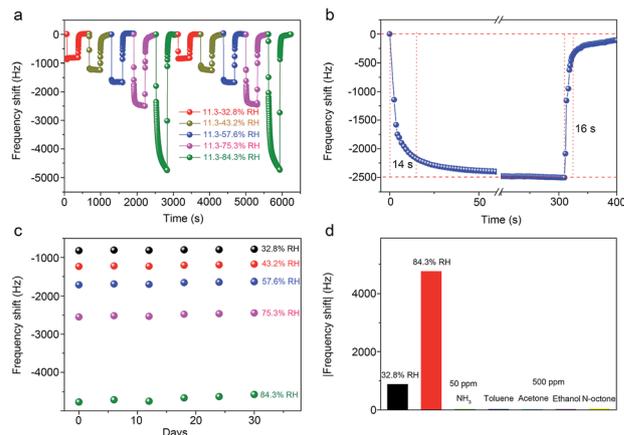

Fig. 8 (a) The dynamic frequency shifts of the QCM-3 transducer. (b) The response and recovery curves between 11.3% and 75.3% conditions. (c) The long-term stability of the sensor. (d) The selectivity of QCM-3 at room temperature.

samples, respectively (with RH levels changing from 11.3% to 84.3%). The QCM-3 sensor has the highest frequency offset (sensitivity). To better understand the performance range of the three humidity sensors, the surface morphologies of the three sensors before and after annealing are given in ESI.† The high-magnification SEM images of QCM-1, QCM-2 and QCM-3 before annealing are shown in Fig. S1a, c and e,† respectively. As shown, the surface morphology of the In$_2$O$_3$ QDs film before annealing gradually become rough with the thickness of the film increasing. After the annealing process, the surface of all the In$_2$O$_3$ QD films turned smooth, with many small cracks (Fig. S1b, d and f†). This porous morphology provides a path for water molecules to diffuse into the interior of the film. Meanwhile, greater amounts of In$_2$O$_3$ QDs have more adsorption sites. Hence, the QCM-3 sensor has high sensitivity to humidity. As shown in Fig. 7b, the frequency response of the three sensors exhibit very good log relationship with humidity, which is consistent with the results of other reported humidity sensors.[38,39] The regression coefficients (R^2) of QCM-1, QCM-2 and QCM-3 sensors are 0.98411, 0.9899 and 0.97367, respectively.
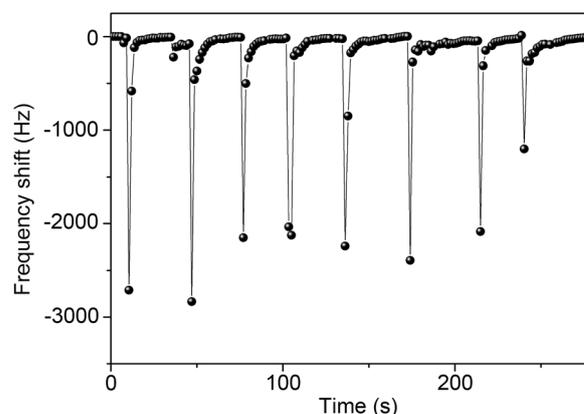

Fig. 9 The frequency response towards human breath from the mouth.

Table 2 The reported humidity sensing performances of QCM sensors

Material	RH range (%)	Sensitivity (Hz per %RH)	Response/recovery time	Ref.
ZnO/GO	11–97	41.10	9/5 s (@63.2%)	11
GQDs–chitosan	11–95	39.2	36/3 s (@95%)	40
SnO_2–SiO_2	11–96	9.4	14/16 s (@90%)	41
ZnO colloid spheres	11–95	77	167.7/8 s (@95%)	42
GO/PEI	11–97	27.3	53/18 s (@90%)	43
GO/SnO_2/PANI	0–97	29.1	7/2 s (@97%)	44
MWCNTs/GO	10–80	9.8	4/3 s (@97%)	45
In_2O_3 QDs	11.3–84.3	56.3	14/16 s (@74.3%)	This work

QCM-3, having the optimal humidity sensitivity, was chosen for further testing. Fig. 8a shows the dynamic frequency changes of the QCM-3 transducer. The sensor was tested twice, with the RH levels changed from 11.3% RH to 32.8% RH, 43.2% RH, 57.6% RH, 75.3% RH and 84.3% RH. The frequency responses did not change significantly under the same humidity conditions, indicating that the humidity sensor has excellent RH measurement repeatability. The response/recovery time is another crucial parameter for evaluating the humidity sensing performance. The response and recovery characteristic curves between the RH levels of 11.3% and 75.3% are shown in Fig. 8b. As can be seen, the response and recovery time of the QCM-3 transducer are 14 s and 16 s, respectively, which indicates the sensor based on In_2O_3 QD film has fast adsorption and desorption characteristics for water molecules. The response/recovery time of QCM-3 under different relative humidity conditions are shown in Fig. S2.† The response time of QCM-3 between 11.3% and 32.8%, 43.2%, 57.6%, 75.3% and 84.3%, were 3 s, 4 s, 3 s, 14 s and 82 s, respectively. Also, the recovery time of QCM-3 between 11.3% and 32.8%, 43.2%, 57.6%, 75.3% and 84.3%, were 19 s, 32 s, 15 s, 16 s and 16 s, respectively. At high relative humidity, physisorption of water molecules will take a longer time to reach equilibrium. Hence, the response time will increase as well. The long-term stability of the humidity sensor is very important for its practical application. Fig. 8c shows the long-term stability of the QCM humidity sensor based on In_2O_3 QDs. The frequency shifts of the sensor do not show apparent changes under different humidity conditions within 30 days. This result indicates that the sensor has good long-term stability. The selectivity testing results of the QCM device are shown in Fig. 8d. It demonstrates that the frequency shifts of the QCM sensor based on In_2O_3 QDs toward water molecules are much higher than those towards the commonly used target gases, including NH_3, ethanol, acetone, toluene, and n-octane. Hence, the sensor has excellent selectivity toward water molecules at room temperature. Finally, we summarized the reported humidity sensing performance of QCM sensors from recent literature (Table 2). The results indicate that our sensor exhibits outstanding sensitivity.

In order to demonstrate the application of QCM sensors based on In_2O_3 QDs for humidity detection, we further measure human breath from the mouth via these sensors. As shown in Fig. 9, breath from the mouth causes a sharp frequency decrease due to the sudden increase of RH level. Hence, the QCM sensor can detect human respiration. These results show that the In_2O_3 QD QCM sensor possesses outstanding sensitivity to humidity and can be used to locate human survivors of disasters.

The humidity sensing mechanism of the In_2O_3 QD QCM humidity sensor depends on adsorption/desorption of water molecules (Fig. 10). Here, In_2O_3 QDs have abundant surface oxygen vacancies and a large specific surface area, which play an important role in improving the sensing performance. First, the chemical absorption of water molecules forms OH^- on the surface of In_2O_3 QDs. Second, more water molecules will be physically adsorbed on the hydroxyl groups through van der Waals forces. As the ambient humidity increases, more water molecules will be adsorbed on the surface of the sensitive film, and the resonant frequency will decrease due to the mass gain of the QCM surface. In contrast, as the environmental RH decreases, water molecules on the surface of the sensitive film are desorbed and released into the environment. Then, the mass loading effect is decreased, and the resonant frequency is increased.

Conclusions

In summary, QCM humidity sensors were fabricated by employing In_2O_3 QDs synthesized using a solvothermal method. In_2O_3 QD films were prepared by spin-coating due to the good solution processing properties, then the films were annealed at 300 °C in order to increase their surface hydrophilicity. This sensor has outstanding sensitivity and short response/recovery times for humidity detection. Meanwhile, the sensor has been used to monitor breath from the mouth, showing its potential for fast humidity detection in practical
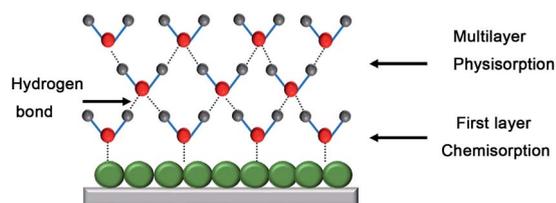

Fig. 10 A schematic diagram of the humidity sensing mechanism of the In_2O_3 QD QCM humidity sensor.

applications. Furthermore, we discussed the humidity sensing mechanisms of this sensor. This study provides a new QD humidity sensing material and expands the application of QDs in QCM humidity sensors.

Conflicts of interest

There are no conflicts to declare.

Acknowledgements

References

1 S. Wei, D. D. Han, L. Guo, Y. Y. He, H. Ding, Y. L. Zhang and F. S. Xiao, *J. Colloid Interface Sci.*, 2014, **431**, 17–23.

2 E. Pál, V. Hornok, R. Kun, A. Oszkó, T. Seemann, I. Dékány and M. Busse, *J. Colloid Interface Sci.*, 2012, **378**, 100–109.

3 P. Tian, X. Y. Gao, G. Wen, L. S. Zhong, Z. Wang and Z. Guo, *J. Colloid Interface Sci.*, 2018, **532**, 517–526.

4 H. Kaden, F. Königer, M. Strømme, G. A. Niklasson and K. Emmerich, *J. Colloid Interface Sci.*, 2013, **411**, 16–26.

5 S. Kano, K. Kim and M. Fujii, *ACS Sens.*, 2017, **2**, 828–833.

6 B. B. Du, D. X. Yang, X. Y. She, Y. Yuan, D. Mao, Y. J. Jiang and F. F. Lu, *Sens. Actuators, B*, 2017, **251**, 180–184.

7 X. H. Le, X. Y. Wang, J. T. Pang, Y. J. Liu, B. Fang, Z. Xu, C. Gao, Y. Xu and J. Xie, *Sens. Actuators, B*, 2018, **255**, 2454–2461.

8 S. Choi, H. Y. Yu, J. Jang, M. Kim, S. Kim, H. S. Jeong and D. Kim, *Small*, 2018, **14**, 1703934.

9 B. Chethan, Y. T. Ravikiran, S. C. Vijayakumari, H. G. Rajprakash and S. Thomas, *Sens. Actuators, B*, 2018, **280**, 466–474.

10 Y. Dong and G. Feng, *Sens. Actuators, B*, 1995, **24**, 62–64.

11 Z. Yuan, H. L. Tai, X. H. Bao, C. H. Liu, Z. B. Ye and Y. D. Jiang, *Mater. Lett.*, 2016, **174**, 28–31.

12 D. Z. Zhang, H. N. Chen, X. Y. Zhou, D. Y. Wang, Y. B. Jin and S. J. Yu, *Sens. Actuators, A*, 2019, **295**, 687–695.

13 J. b. Lin, N. B. Gao, J. M. Liu, Z. X. Hu, H. Fang, X. H. Tan, H. Y. Li, H. Jiang, H. Liu, T. L. Shi and G. L. Liao, *J. Mater. Chem. A*, 2019, **7**, 9068.

14 D. Z. Zhang, C. X. Jiang and J. F. Wu, *Sens. Actuators, B*, 2018, **273**, 176–184.

15 X. L. Cha, F. F. Yu, Y. Fan, J. F. Chen, L. Y. Wang, Q. Xiang, Z. M. Duan and J. Q. Xu, *Sens. Actuators, B*, 2018, **263**, 436–444.

16 D. Z. Zhang, H. N. Chen, P. Li, D. Y. Wang and Z. M. Yang, *IEEE Sens. J.*, 2019, **19**, 2909–2915.

17 E. S. Muckley, L. Collins, A. V. Ievlev, X. Y. Ye, K. Kisslinger, B. G. Sumpter, N. V. Lavrik, C. Y. Nam and I. N. Ivanov, *ACS Appl. Mater. Interfaces*, 2018, **10**, 31745–31754.

18 N. B. Gao, H. Y. Li, W. H. Zhang, Y. Z. Zhang, Y. Zeng, Z. X. Hu, J. Y. Liu, J. J. Jiang, L. Miao, F. Yi and H. Liu, *Sens. Actuators, B*, 2019, **293**, 129–135.

19 M. A. Mahjoub, G. Monier, C. R. Goumet, F. Reveret, M. Echabaane, D. Chaudanson, M. Petit, L. Bideux and B. Gruzza, *J. Phys. Chem. C*, 2016, **120**, 11652–11662.

20 Z. Q. Wei, Z. K. Zhou, Q. Y. Li, J. C. Xue, A. D. Falco, Z. J. Yang, J. H. Zhou and X. H. Wang, *Small*, 2017, **13**, 1700109.

21 C. Melios, A. Centeno, A. Zurutuza, V. Panchal, C. E. Giusca, S. Spencer, S. P. Silva and O. Kazakova, *Carbon*, 2016, **103**, 273–280.

22 L. T. Duy, T. Q. Trung, V. Q. Dang, B. Hwang, S. Siddiqui, I. Y. Son, S. K. Yoon, D. J. Chung and N. E. Lee, *Adv. Funct. Mater.*, 2016, **26**, 4329–4338.

23 P. Yasaei, A. Behranginia, T. Foroozan, M. Asadi, K. Kim, F. K. Araghi and A. S. Khojin, *ACS Nano*, 2015, **9**, 9898–9905.

24 M. B. Erande, M. S. Pawar and D. J. Late, *ACS Appl. Mater. Interfaces*, 2016, **8**, 11548–11556.

25 S. H. Wu, G. H. Wang, Z. Xue, F. Ge, G. B. Zhang, H. B. Lu and L. Z. Qiu, *ACS Appl. Mater. Interfaces*, 2017, **9**, 14974–14982.

26 D. Z. Zhang, D. Y. Wang, P. Li, X. Y. Zhou, X. Q. Zong and G. K. Dong, *Sens. Actuators, B*, 2018, **255**, 1869–1877.

27 T. Alizadeh and M. Shokri, *Sens. Actuators, B*, 2016, **222**, 728–734.

28 Z. Lu, Y. Q. Gong, X. J. Li and Y. Zhang, *Appl. Surf. Sci.*, 2017, **399**, 330–336.

29 S. Yadav, P. Chaudhary, K. N. Uttam, A. Varma, M. Vashistha and B. C. Yadav, *Nanotechnology*, 2019, **30**, 295501.

30 C. Y. Zhu, F. Xu, L. Zhang, M. L. Li, J. Chen, S. H. Xu, G. G. Huang, W. H. Chen and L. T. Sun, *Chem.–Eur. J.*, 2016, **22**, 7357–7362.

31 Z. S. Hosseini, A. Iraji zad, M. A. Ghiass, S. Fardindoost and S. Hatamie, *J. Mater. Chem. C*, 2017, **5**, 8966.

32 N. Sakly, A. H. Said and H. B. Ouada, *Mater. Sci. Semicond. Process.*, 2014, **27**, 130–139.

33 E. Selishcheva, J. Parisi and J. Kolny-Olesiak, *J. Nanopart. Res.*, 2012, **14**, 711.

34 Y. Yu, X. Guan, X. Li, W. Li, L. Jiang and D. Chen, *J. Alloys Compd.*, 2016, **672**, 265–270.

35 C. Liang, G. Meng, Y. Lei, F. Phillipp and L. Zhang, *Adv. Mater.*, 2010, **13**, 1330–1333.

36 E. Selishcheva, J. Parisi and J. Kolny-Olesiak, *J. Nanopart. Res.*, 2012, **14**, 711.

37 X. Xu, J. Zhuang and X. Wang, *J. Am. Chem. Soc.*, 2008, **130**, 12527–12535.

38 X. Zhou, J. Zhang, T. Jiang, X. Wang and Z. Zhu, *Sens. Actuators, A*, 2007, **135**, 209–214.

39 X. Wang, B. Ding, J. Yu, M. Wang and F. Pan, *Nanotechnology*, 2010, **21**, 055502.

40 P. J. Qi, T. Zhang, J. R. Shao, B. Yang, T. Fei and R. Wang, *Sens. Actuators, B*, 2019, **287**, 93–101.

41 Y. Zhu, J. C. Chen, H. M. Li, Y. H. Zhu and J. Q. Xu, *Sens. Actuators, B*, 2014, **193**, 320–325.

42 J. Xie, H. Wang, Y. H. Lin, Y. Zhou and Y. P. Wu, *Sens. Actuators, B*, 2013, **177**, 1083–1088.

43 Z. Yuan, H. Tai, Z. Ye, C. Liu, G. Xie, X. Du and Y. D. Jiang, *Sens. Actuators, B*, 2016, **234**, 145–154.

44 D. Z. Zhang, D. Y. Wang, X. Q. Zong, G. K. Dong and Y. Zhang, *Sens. Actuators, B*, 2018, **262**, 531–541.

45 X. Y. Li, X. D. Chen, Y. Yao, N. Li, X. P. Chen and X. Bi, *IEEE Sens. J.*, 2013, **13**, 4749–4756.